Fluorescence Nanometrology in Sol-Gels

D.J.S. BIRCH, C.D. GEDDES, J. KAROLIN, R. LEISHMAN, AND O.J. ROLINSKI

We describe recent fluorescence studies of the formation dynamics and structure of sol-gel glasses from nanometre particles composed of silica clusters in sols to nanometre pores in silica gels. The "kinetic life-history" of silica produced under both acidic and alkaline conditions from sodium silicate in a hydrogel and from an alkoxide in an alcogel is now starting to be revealed by fluorescence techniques and the influence of key parameters such as pH and silica concentration quantified at the molecular level. Through careful choice of fluoro-probe, anisotropy decay has been shown to provide particle size as well as viscosity information and offer advantages over traditional techniques for silica particle sizing based on small angle neutron, X-ray or light scattering. Fluorescence resonance energy transfer (FRET) can now be used to determine the donor-acceptor spatial distribution function without making any *a-priori* assumptions as to its form. This in turn promises to make FRET a better means of monitoring pore morphology in the wet gel during drying and ageing, offering distinct advantages over dry gel techniques such as mercury porosimetry and nitrogen adsorption. The insight into sol-gel processes provided by these new interpretations of fluorescence decay data promises to have implications for both our fundamental understanding and the production of sol-gel systems.

3.1 Introduction

Fluorescence resonance energy transfer (FRET) is often cited as being "an Å ruler" or "spectroscopic ruler" and these phrases highlight one of the prime features of modern day fluorescence spectroscopy, namely the resolution for reporting on molecular structure and dynamics at a functional level. FRET works fine over ~10 to 100 Å, but of course fluorescence anisotropy decay can also provide a distance measurement via the hydrodynamic radius. In this chapter we consider recent work combining these two powerful fluorescence techniques in an area of metrology aimed at unravelling the molecular mysteries leading up to the silica sol to gel transition and beyond.

The silica sol-gel process is a room temperature polymerisation whereby the precursor solution "*the sol*" forms a rigid network spanning the containing vessel, after a time t_g [1]. This point marks the onset of "*the gel*" and t_g is strongly pH, temperature and silica concentration dependent. Prior to t_g ramified nanometre size clusters of silica form and diffuse. Eventually, this process leads to the rigid network appearing at t_g and other processes start to dominate as the solvent evaporates, pores form as the particles aggregate, condensation occurs and the gel shrinks (syneresis) and ages. Although the chemistry is in general well understood the complexity of physics can be gauged from the fact that many of the chemical processes occur simultaneously, not sequentially, although at different times different reaction rates may dominate. For example, for a while even after t_g most of the volume is still a liquid. Control of the polymerisation produces a wide range of materials. These include stable colloids of well defined nanoparticles, e.g., Dupont's Ludox (which has many uses though known in fluorescence as a light scattering medium for recording excitation pulse profiles), optical quality components used in photonics, porous glasses used in sensors and the ubiquitous uses of silica gel powder.

A clearer picture of how controlling the competitive rates in the sol in the very early stages translate into the final gel is not only important to our fundamental understanding, but also in optimising manufacturing processes. The link between particle size in the sol and pore size in the gel is a classic example, which spans the whole "life-history" of silica gel. Of course any technique for monitoring such changes should ideally be capable of monitoring *in-situ* the whole process through to completion. Fluorescence is *par excellence* a method of determining reaction rates and, although ideally suited to the task in sol-gels, its capabilities have perhaps been hitherto under-appreciated in this context.

Traditionally, small angle scattering of laser light, X-rays or neutrons have been used to study silica particle growth. For example, light scattering measurements found a primary particle hydrodynamic diameter of 1.0 nm increasing to 2.4 nm prior to gelation [2]. Small angle X-ray scattering studies of silica gel have revealed evidence for 1 nm particles [3] and similar studies on a silica sol indicate that 2 nm diameter primary particles aggregate to form secondary particles of 6 nm diameter prior to gelation [4]. Small angle neutron scattering has found com-

parable primary particle dimensions [5]. However, scattering methods have a number of drawbacks. For example, they need low silicate concentrations to avoid multiple scattering and dilution is not the answer, as this can cause depolymerisation. Moreover, scattering by the gel matrix after t_g corrupts the particle scattering measurement. X-ray and neutron scattering in particular are also very expensive and unsuitable for on-line use. Light scattering is limited in resolution by the wavelength of light and electron microscopy can only be used on dry colloids.

Fluorescence correlation spectroscopy (FCS) [6] and fluorescence recovery after photobleaching (FRAP) [7] possess sufficient resolution for silica particle metrology, but also suffer from the need to dilute the sols and have the added complication of requiring a microscope.

We include in this chapter the use of fluorescence anisotropy decay to determine the growth in hydrodynamic radius of silica particles [8, 9]. Although fluorescence anisotropy decay has been widely used in biochemistry to determine structure and dynamics in membranes and proteins [10] it has hitherto found little if any application where the hydrodynamic radius of the fluorescing rotor species changes continuously with time. And yet fluorescence anisotropy decay is ideally suited to particle metrology during sol-gel polymerisation, overcoming many of the drawbacks of scattering methods. For example, because in the absence of energy migration fluorescence anisotropy will decay only by rotating particles, growth can be studied at higher silicate concentrations than other techniques and even after gelation has occurred. Interestingly, although fluorescence has been widely used to study the sol to gel transition the interpretation was for a long time confined to viscosity [11–15]. The realisation that the observed second and longer rotational correlation time corresponded to dye bound to particles [8, 9] has bridged the gap between scattering and fluorescence techniques and is providing new insight into silica growth mechanisms.

Fluorescence also has much to offer in gel studies after t_g. Traditional techniques for pore size and surface area measurement such as mercury porosimetry, nitrogen adsorption, and BET analysis can only be used on dry gels [1]. FRET has demonstrable capabilities for studying wet gels *in-situ*. The dual assumptions of a random donor-acceptor distance distribution function for $\rho(r)$ in a specific geometry such as a cylinder, sphere or fractal enables the donor fluorescence decay to be analysed and pore size estimates determined [16–19]. Recently, we have started to apply a new approach to the problem whereby $\rho(r)$ is determined from fluorescence decay measurements without making any *a-priori* assumptions as to its form and changes in pore morphology are then analysed by applying the single assumption of a specific geometrical model. The theoretical basis of finding $\rho(r)$ [20] has been shown to work well in describing the discrete acceptor binding sites found in a protein [21–23] and the porous polymer Nafion used in FRET based metal ion sensing [24], which is in some ways analogous to sol-gel pores. In this chapter we show that in a sol-gel not only pore diameters, but also wall thickness between pores can be obtained by determining (i.e., not assuming) a form for $\rho(r)$.

The combination of fluorescence anisotropy and FRET enables the "kinetic life-history" of silica gel to be tracked *in-situ* from particle to pore. Fig. 3.1 de-

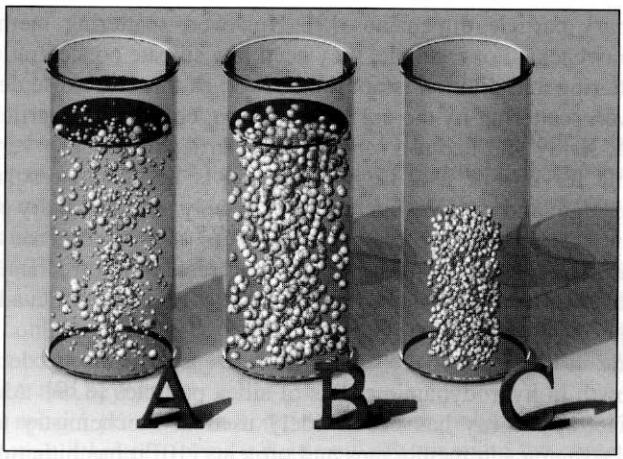

Fig. 3.1. Generalised depiction of the sol to gel transition in silica gel. **A** Nanometre scale particles composed of clusters of silica form and join together to form a growing network (**B**), which spans the containing vessel at a time t_g and then shrinks forming pores (**C**)

picts the problem, which we will expand upon in terms of critical parameters in the sol, such as pH and silica concentration through illustrative examples.

3.2 Sol-gel Chemistry

The sol-gel process involves the transformation of a liquid like solution, *the sol*, to *the gel*, a highly porous matrix filled with solvent, through a series of hydrolysis and polycondensation steps.

Simplified the gel-forming step can be given by:

$$n\ \mathrm{Si(OR)_4} + 2\ n\ \mathrm{H_2O} \rightarrow n\ \mathrm{SiO_2}\ \text{(a growing gel network)} + 4\ n\ \mathrm{ROH} \qquad (3.1)$$

where R is hydrogen for the case of hydrogels (an inorganic polymerisation) and methyl or ethyl or propyl etc (an organic polymerisation) for the case of alcogels, both so named in accordance with the solvents used and condensed. The rates of formation and properties of the final gels derived from these organic and inorganic polymerisations are strongly pH, temperature, solvent and SiO_2 concentration dependent [1, 25]. There are many similarities between both processes and similar end products are obtained. The alkoxide "alcogel" route is the one that has been mostly used for research into sol-gel processes because it has better defined reactants and is typically simpler to prepare than a hydrogel; the lower cost of the latter making it ideal for industrial applications requiring mass production.

For hydrogels at pH < 2 (acid catalysed), gelation is thought to occur by means of rapid monomer additions initially to form primary clusters followed by intercluster condensation reactions between silanol (Si-OH) bonds to form ramified si-

loxane type (Si-O-Si) secondary clusters [1]. For hydrogels polymerised from sodium silicate solution (water glass), a ternary system of SiO_2, Na_2O and H_2O, then the gel-forming step can be crudely described by:

$$Na_2O \cdot x\ SiO2 \cdot Y\ H_2O\ (\text{water glass}) + H_2SO_4 \rightarrow SiO_2 + Na_2SO_4 + (Y+1)H_2O \quad (3.2)$$

where x denotes the weight ratio (w/w) of the glass, i.e., SiO_2:Na_2O, which for the work described here is ≈ 3.3. At a sol pH < 2, the gel times are typically quite long (Fig. 3.2) where the polymerisation rate is thought to be proportional to $[H^+]$ and the silicate species are thought to be positively charged but not highly ionised [25]. Also, in the absence of fluoride ions, the solubility of silica below pH 2 is quite low. It is therefore likely [1] that the formation and aggregation of primary particles occurs rapidly together and that Ostwald ripening (a process whereby particles grow in size but decrease in number as highly soluble small particles dissolve and reprecipitate on larger less soluble nuclei) contributes little to particle growth after the particles exceed 1 nm radius. Therefore, gels polymerised at pH < 2 are thought to be comprised of the joining together of very small particles indeed.

At intermediate sol pH of 2–6 (Fig. 3.2), the gel times steadily decrease and it is thought that above the isoelectric point at around pH 2 the condensation rate is proportional to $[OH^-]$ as shown below [1].

$$\equiv Si\text{-}OH + OH^- \rightarrow \equiv Si\text{-}O^- + H_2O \quad \text{(Fast process)} \quad (3.3)$$

$$\equiv Si\text{-}O^- + HO\text{-}Si \rightarrow \equiv Si\text{-}O\text{-}Si\equiv + OH^- \quad \text{(Slower process)} \quad (3.4)$$

At a pH above 7, hydrogel sol polymerisation occurs by the same nucleophilic mechanism as for sols in the pH range 2–7, Eqs. 3.3 and 3.4. However, because all condensed species are likely to be negatively charged (highly ionised) and therefore mutually repulsive, growth occurs primarily by the addition of monomers to more highly condensed particles *rather* than by particle aggregation [1]. Particles

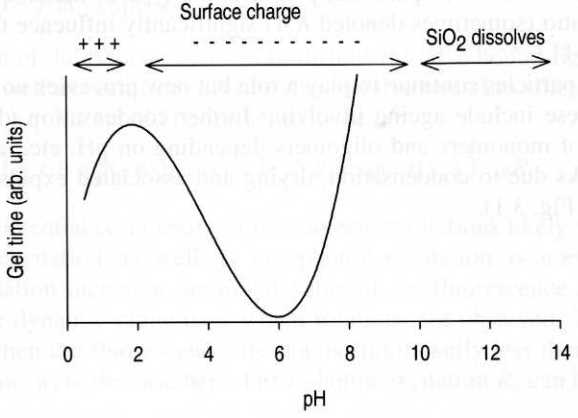

Fig. 3.2. Effect of pH on gel time and sol stability (adapted from [25])

of ≈1 nm radii are typically formed within a few minutes above pH 7. Due to the greater solubility of silica and the greater size dependence of solubility above pH 7, the growth of primary particles continues by Oswald ripening. At a given pH, particles grow to a size that depends mainly on the temperature and SiO_2 concentration, with the *growth rate* also depending on the particle size distribution. Due to lack of salt and the mutually repulsive nature of the silica particles, stable, fairly high pH, non-gelling sols can be readily prepared [25] (Fig. 3.2), e.g., DuPont's colloidal silica range. At a much higher sol pH, ≥ 12, most silanol groups are deprotonated and the primary building blocks are composed primarily of cyclic trimers and tetramers.

The alkoxide "alcogel" route, which is similar in many respects to the polymerisation of aqueous silicates, can be described at the functional group level by three simple reactions [1]:

$$Si(OR)_4 + n\,H_2O \leftrightarrow Si(OR)_{4-n}(OH)_n + n\,ROH \quad \text{Hydrolysis} \tag{3.5}$$

$$\equiv Si\text{-}OR + HO\text{-}Si\equiv \leftrightarrow \equiv Si\text{-}O\text{-}Si\equiv + ROH \quad \text{Alcohol Condensation} \tag{3.6}$$

$$\equiv Si\text{-}OH + HO\text{-}Si\equiv \leftrightarrow \equiv Si\text{-}O\text{-}Si\equiv + H_2O \quad \text{Water Condensation} \tag{3.7}$$

and overall in the case of tetramethylorthosilicate (TMOS) reported here by:

$$n\,Si(OCH_3)_4 + 2\,n\,H_2O \rightarrow n\,SiO_2 + 4\,n\,CH_3OH \quad \text{Net Reaction} \tag{3.8}$$

The hydrolysis reaction, Eq. 3.5, effectively replaces alkoxide groups with hydroxyl groups, which can then readily condense to produce either water, Eq. 3.7, or alcohol, Eq. 3.6, where both reactions result in siloxane (Si-O-Si) bonds. Due to the fact that water and alkoxides are immiscible, a mutual solvent is typically used as a homogenising agent, e.g., an alcohol. As indicated by Eqs. 3.5 and 3.6, alcohol is not just a solvent but can participate in the reverse esterification and alcoholysis reactions, respectively. The hydrolysis scheme, Eq. 3.5, is generally acid or base catalysed where the rate and nature of polymerisation is pH dependent [1]. Other parameters such as temperature, pressure, the type of alcohol used and the molar H_2O:Si ratio (sometimes denoted R:1) significantly influence the properties of the final gel [1].

Even after t_g particles continue to play a role but new processes now start to occur as well. These include ageing involving further condensation, dissolution or reprecipitation of monomers and oligomers depending on pH, etc., and syneresis as the gel shrinks due to condensation, drying and associated expulsion of liquid from pores (see Fig. 3.1).

3.3 Anisotropy Theory

Vertically and horizontally polarised fluorescence decay curves, $F_V(t)$ and $F_H(t)$, orthogonal to pulsed and vertically polarised excitation, recorded at different delay times following initial mixing of the sol, lead to an anisotropy function $R(t)$ [10] describing the rotational correlation function where:

$$R(t) = \frac{F_V(t) - F_H(t)}{F_V(t) + 2\,F_H(t)} \tag{3.9}$$

If continuous excitation is used the time-dependencies remain unresolved and a weighted average of the individual time-resolved anisotropies is observed in a multi-component system such as a sol-gel.

Our previous analysis of $R(t)$ [8, 9] for silica hydrogels and that of Narang and coworkers [14] on TMOS showed that the best description was provided by two rotational correlation times τ_{r1} and τ_{r2} in the form:

$$R(t) = (1-f)R_0 \exp(-t/\tau_{r1}) + f\,R_0 \exp(-t/\tau_{r2}) \tag{3.10}$$

where R_0 is the initial anisotropy. We interpret 'f' as the fraction of fluorescence due to probe molecules bound to silica particles and hence $1-f$ the fraction due to free dye in the sol. From the Stokes-Einstein relation, τ_{r1} gives the sol microviscosity $\eta_l = 3\tau_{r1}kT/4\pi r^3$, where r is the hydrodynamic radius of the dye and likewise using η_l and τ_{r2} gives the average silica particle hydrodynamic radius.

By expanding $\exp(-t/\tau_{r2})$ and putting $\tau_{r1} << \tau_{r2}$, to reflect the unbound probe molecules rotating much faster than those which are bound to silica particles, then in the case where the fluorescence lifetime $\tau_f << \tau_{r2}$ a similar expression to that encountered for the hindered rotation of a fluorophore in a membrane or protein [10] can be expected to hold in a sol-gel, i.e., a residual anisotropy is observed:

$$R(t) = (1-f)R_0 \exp(-t/\tau_{r1}) + f\,R_0 \tag{3.11}$$

If a fraction of the fluorescence 'g' is attributed to dye bound rigidly within the gel after t_g as well as both free solvated dye and dye bound to silica particles then, if appropriate, Eq. 3.10 could be further extended to

$$R(t) = (1-f-g)R_0 \exp(-t/\tau_{r1}) + f\,R_0 \exp(-t/\tau_{r2}) + gR_0 \tag{3.12}$$

Given the potential complexity of the molecular rotations likely to be observed, multiphoton excitation as well as one-photon excitation is useful [26]. Multiphoton excitation increases the initial value of the fluorescence anisotropy, R_0, and hence the dynamic range over which rotations are observed. This is particularly useful when the fluorescence lifetime is significantly less than the rotational correlation time, as is the case here. For i-photon excitation R_0 can be expressed as [26]:

$$R_{0i} = \frac{2i}{2i+3}\left[\frac{3}{2}cos^2\beta_i - \frac{1}{2}\right] \tag{3.13}$$

where β_i is the intramolecular angle between the dominant absorption and emission transition moments. In the collinear ($\beta_i = 0$) case, $R_{0i} = 0.4$ for $i = 1$ and 0.57 for $i = 2$.

3.4 FRET Donor-acceptor Distribution Theory

Among several molecular mechanisms which can be applied to the detection of a structure of a complex media, FRET from the excited donor molecule D to the acceptor molecule A provides quite specific site (and hence structural) information. This is because the rate of FRET, w(r), is

$$w(r) = (1/\tau_0)(D_0/r)^6 \tag{3.14}$$

and depends strongly on the donor/acceptor spectral characteristics (D_0 being a measure of donor fluorescence and acceptor absorption spectral overlap), providing potential for high selectivity, but also on the donor-acceptor distance r. τ_0 is the donor fluorescence lifetime in the absence of FRET, and D_0 is defined as the critical transfer distance at which the probability of FRET is ½ and is specific for each donor-acceptor pair.

In the presence of an acceptor the donor fluorescence impulse response function $I_D(t)$ is modified from a monoexponential function $exp(-t/\tau_0)$ to the form [20]:

$$I_D(t) = \exp\left[-\frac{t}{\tau_0} - \int_0^\infty dr\, \rho(r)(1-\exp[-tw(r)])\right] \tag{3.15}$$

Here $\rho(r)$ is the donor-acceptor distribution function, where $\int_0^R \rho(r)dr$ is the number of acceptor molecules in a volume of a sphere of radius R.

Equation 3.15 constitutes an inverse problem in which the donor-acceptor distribution function $\rho(r)$ is an input information which is to be recovered from the output signal $I_D(t)$. The transmitted information might be modified during measurements by the detection method applied, autofluorescence and scatter.

Problems similar to that posed by Eq. 3.15 arise in a wide variety of biochemical and porous solid applications, and consist of using mathematical models in order to determine unknown system inputs, sources or parameters from observed system outputs and responses. A common approach is to use a mathematical model to fit, often using least-squares error analysis, predictions of the model to the measured system outputs by adjusting the unknown model parameters. For example, the integral in Eq. 3.15 is usually solved for the assumed random 3 or 2-dimensional distribution $\rho(r)$ and the parameter γ, indicating the acceptor concen-

tration, is determined from the experimental data. This simple approach is not appropriate to systems of complex structures.

Mathematically, Eq. 3.15 belongs to a class of Fredholm integral equations of the first kind, which are known to be ill-posed. This means that the solution $\rho(r)$ may not be unique, may not exist and may not depend continuously on the data. The extent of such problems mainly depends on the property of the integral kernel, which, together with the accuracy of the fluorescence impulse response function measurement $I_D(t)$ and smoothing techniques, will determine how much information about $\rho(r)$ can be extracted from the measurements. In this approach the donor-acceptor distribution function $\rho(r)>0$ is expressed as the infinite series of the orthonormal Laguerre polynomials $L_k^s(r)$ with the coefficients $a_k^{(s)}$ without sacrificing generality of the function $\rho(r)$:

$$\rho(r) = r^5 \sum_{k=0}^{\infty} a_k^{(s)} L_k^s(r) \tag{3.16}$$

where s is an arbitrary chosen parameter. Combining Eq. 3.16 and Eq. 3.15 and then applying to both sides of the resulting expression the operator:

$$\int_0^{\infty} dt e^{-t} L_V(t)* \tag{3.17}$$

defined in time space, we obtain:

$$f_{\alpha,p} = \sum_{k=0}^{m} a_k^{(s)} b_{kp}^s(\alpha) \tag{3.18}$$

Equation 3.18 establishes fundamental relationship between the experimentally available vector $f_\alpha = \{f_{\alpha,0}, f_{\alpha,1}, f_{\alpha,2},\ldots,f_{\alpha,p}\}$ defined in the time domain, the sought for vector $a^{(s)} = \{a^s_0, a^s_1, a^s_2,\ldots,a^s_M\}$ defined in the distance domain, and the matrix $b^{(s)}(\alpha)$, which depends on $\alpha = D_0^6/\tau_0$ only. The basic procedure for determining of $\rho(r)$ in this approach assumes several steps. In the first step the parameter α is estimated from the steady-state (D_0) and time-resolved (τ_0) measurements. Next, the donor-acceptor system for which $\rho(r)$ is to be determined is prepared, the donor fluorescence decay is measured and the f_α vector calculated. In the next step the mode of representation of the donor-acceptor distribution function (s value) has to be chosen and the matrix $b^{(s)}(\alpha)$ calculated. Finally, vector $a^{(s)}$ is found from solving the set of Eq. 3.18 and $\rho(r)$ is calculated on the basis of Eq. 3.16. The donor/acceptor pair of particular D_0 value reports only the value of $\rho(r)$ in the narrow region ($D_0 - dD_0$, $D_0 + dD_0$) [20]. Thus, improved accuracy of $\rho(r)$ requires the measurements to be made over a range of D_0 values. Here we will report only $\rho(D_0)$ determination on a shrinking gel at a single D_0 value. However, recently [23] we have shown how $\rho(r)$ can be determined in the range for $0 < r < 2\ D_0$ for a glucose-binding protein and work is currently underway to apply this approach to sol-gels.

3.5 Acidic Hydrogels

Fig. 3.3 shows a typical silica particle growth and microviscosity at pH < 1 for a hydrogel using an analysis of anisotropy decays according to Eq. 3.10. Under such strongly acidic conditions (c.f. Eq. 3.2) many dyes are unstable but the cationic dye JA120 [27] was used successfully as a probe (radius 0.75 nm) and excited at 650 nm using a diode laser of 50 ps pulses at 1 MHz repetition rate and time-correlated single-photon timing detection [28]. Working in the near-infrared overcomes the sol auto-fluorescence but places a further restriction on the choice of dye. Polarized fluorescence decays were accumulated for 1 minute durations during polymerisation. At pH < 1 the particles are slightly positively charged and hence a cationic dye is only slowly taken up by the silica particles such that both the microviscosity and the particle radius can be determined together experimentally using Eq. 3.10. Notable features include the constancy of the microviscosity in the range 1–2 cP, the reducing growth rate as the particle number density decrease as particles bind and grow via inter-particle condensation reactions (e.g., Eq. 3.7) and particle syneresis due to intra-particle condensation. The initial growth kinetics are well described for a particle radius r by:

$$r = r_0 + (r_{max} - r_0)\,(1 - e^{-kt}) \tag{3.19}$$

Modelling such as Fig. 3.3 quantifies a number of key parameters in sol-gel kinetics. A growth rate $k \sim 8.6 \times 10^{-5}$ s^{-1} at early times is seen to dominate over a syneresis rate $\sim 6 \times 10^{-6}$ s^{-1} until later times. The fluorescence evidence is consistent with other evidence [1, 25]. At very early times silicic acid monomer units rapidly combine under diffusion control (i.e., the probability of collisions producing binding approaches unity) to form primary particles of mean hydrodynamic radius 1.5–2 nm, which then aggregate under chemical reaction control (i.e., the collisional binding probability is significantly less than unity) and grow ~ 3 fold to

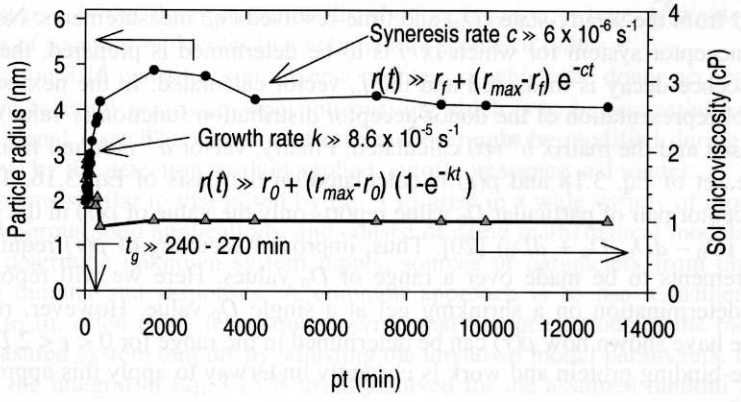

Fig. 3.3. Typical silica hydrogel particle growth and sol microviscosity at pH < 1 during a polymerisation time pt

produce secondary clusters of 4–5 nm maximum mean radius. Simple geometrical considerations predict that a secondary particle contains ~13 primary particles. These trends have been confirmed over a wide range of sols at pH < 1 [8, 9]. The formation of the primary particles is too fast to be resolved under these conditions.

3.6 Alkaline Hydrogels

Moving now to the alkaline region of stability at higher pH. Once again the extreme pH can cause dye instability, in this case deprotonation, but using rhodamine 700 as a probe Fig. 3.4 shows the particle growth kinetics at pH 10 assuming a microviscosity of 1 cp. This pH region represents destabilisation of the initial silicate (pH ≥ 13) to produce gelation under alkaline conditions and consequently, the particles would be expected to be highly negatively charged and mutually repulsive. Hence, unlike at low pH < 1, growth at high pH would be expected to be more by monomer addition and Ostwald ripening rather than particle aggregation [1, 25]. Fig. 3.4 obtained at pH 10 shows a dramatic difference from Fig. 3.3 at pH 0.9 in respect of the former showing a clear bi-modal growth. We have modelled the particle growth in Fig. 3.4 successfully using a function of the form:

$$r = r_0 + (r_p - r_0)(1 - \exp[-k_p t]) + (r_s - r_p)(1 - \exp[-k_s t]) \tag{3.20}$$

This function implies the growth of two different entities, one a precursor to the other, which reach different limiting radii r_p and r_s. Conventional thinking would ascribe k_p as the rate of growth of a primary particle species due to monomer addition and k_s as the growth of secondary particles, again by monomer addition, all slowed up sufficiently to be measurable by the mutual negative repulsive charge causing reaction limiting conditions. However, a single growth mechanism begs the question as to why two entities with distinct rates of formation are observed at

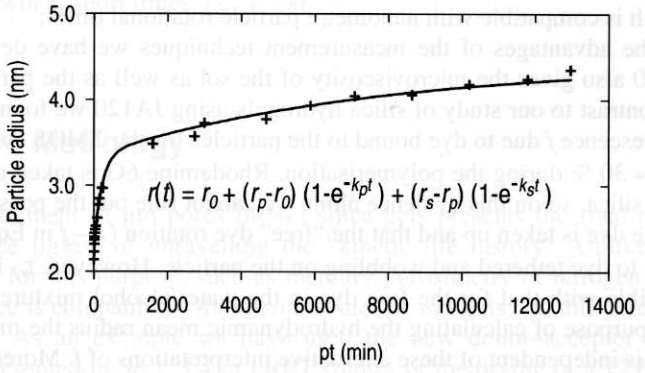

Fig. 3.4. Silica hydrogel particle growth at pH 10 for a 2% SiO_2 sol of t_g > 250 hr during a polymerisation time pt

all and from the fluorescence evidence the role of cluster-cluster aggregation cannot be ruled out, particularly at early times, since the growth rate (k_p) is close to that of 8.6×10^{-5} s^{-1} observed for secondary particles under acidic conditions at pH < 1 (see Fig. 3.3).

Fitting to Eq. 3.20 gives r_0 = 2.3 nm, r_p= 3.3 nm, r_s= 4.6 nm, k_p= 9.2×10^{-5} s^{-1} and k_s = 1.9×10^{-6} s^{-1}. According to this model r_0 simply reflects the mean primary particle size in our first measurement. k_s is just less than the syneresis rate measured under acidic conditions (from Fig. 3.3 ~ 6×10^{-6} s^{-1}) and might reflect a net growth limited by intra-particle syneresis.

3.7 Alkoxide Alcogels

As was already mentioned the alkoxide "alcogel" route (Eqs. 3.5–3.8) is the one that has been mostly used for research into sol-gel processes because it has better defined reactants and is typically simpler to prepare than the hydrogel route. The polymerisation of tetramethyl-orthosilicate (TMOS) has been studied previously using rhodamine 6G [14] and phase fluorometry and the anisotropy decay interpreted solely in terms of viscosity changes. We have recently re-investigated this system using a slowly gelling 21.9 % (*w/w*) SiO_2 sol at pH 2.3, i.e., close to the iso-electric point (c.f. Fig. 3.2 and [29]). At 20° C t_g is ~ 6 x 10^4 min and this gives plenty of time to maximise the anisotropy statistical precision during measurements in which negligible sol changes occur. The measurement precision was further enhanced by using a fluorometer capable of two-photon excitation, increasing the initial anisotropy (c.f. Eq. 3.13 and [30]). Rhodamine 6G seems to be as close as possible to an ideal dye for this type of work. The merits of rhodamine 6G are that it is stable over a wide pH range (~1–12), is highly fluorescent, has a high two-photon absorption cross-section [31, 32] and R_{02} ~ 0.5 [30], is a well characterized isotropic rotor, is readily taken up by silica and has a fluorescence lifetime ≈ 4 ns, which is compatible with nanometre particle rotational times.

One of the advantages of the measurement techniques we have developed is that Eq. 3.10 also gives the microviscosity of the sol as well as the particle mean radius. In contrast to our study of silica hydrogels using JA120 we found the fraction of fluorescence f due to dye bound to the particles for the TMOS sol remained constant at ≈ 30 % during the polymerisation. Rhodamine 6G is taken up very efficiently by silica, so on this evidence alone we cannot rule out the possibility that in fact all the dye is taken up and that the "free" dye rotation ($1 - f$ in Eq. 3.10) actually refers to dye tethered and wobbling on the particle. However, τ_{r1} is ~300 ps, i.e., compatible with that for the free dye in the water/alcohol mixture in the sol and for the purpose of calculating the hydrodynamic mean radius the model given by Eq. 3.10 is independent of these alternative interpretations of f. Moreover, since $r \sim \eta^{-3}$ the viscosity value used is less critical. Here we have used the viscosity determined from τ_{r1} assuming the theoretical hydrodynamic radius for rhodamine 6G

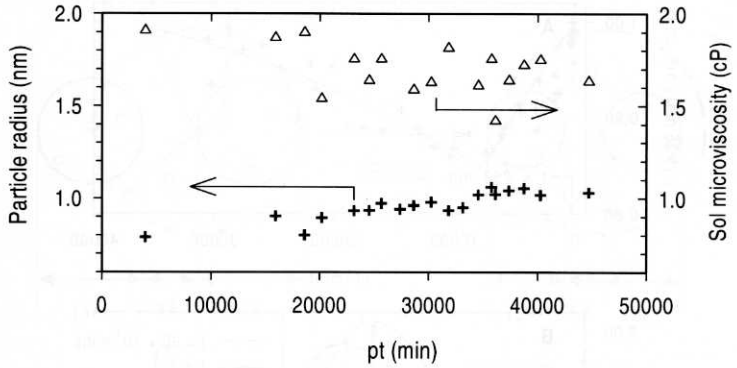

Fig. 3.5. Silica particle radius, +, and sol microviscosity, Δ, as a function of polymerisation time, pt, for a 21.9 % (w/w) SiO_2 TMOS sol at pH 2.3. The errors in particle radius were typically ± 0.1 nm

of 0.56 nm [33, 14]. Our own study of rhodamine 6G in a range of known viscosity solvents gave a consistent hydrodynamic radius of 0.53 ± 0.03 nm.

Fig. 3.5 shows how the calculated viscosity and particle mean radius change with polymerisation time, pt. The viscosity values are similar in magnitude and show a slight downward trend with time, similar to that shown in Fig. 3.3 for a silica hydrogel [8, 9] at low pH, reflecting here the polymerisation of the sol and the expulsion of methanol. The most notable feature of Fig. 3.5 is the smaller radius than anything we have so far detected, growing from ~ 0.8 to 1.1 nm and illustrating the high-resolution fluorescence anisotropy can offer. Clearly the small size reflects the different growth mechanism associated with monomer-monomer and monomer-particle addition in TMOS under these conditions rather than secondary particle aggregation. We fitted the growth of silica hydrogels at pH < 1 to a radius $r \sim 1 - e^{-kt}$ and attributed this to particle-particle aggregation. For TMOS under these conditions Fig. 3.5 can clearly be approximated by the limit of slow exponential growth at short times, i.e., $r \sim kt$.

3.8 Wet Pore Metrology

The measurement of nm pores in wet silica gels presents the final piece in the fluorescence jigsaw of unravelling the "kinetic life history". Unlike traditional techniques for this purpose, such as mercury porosimetry or nitrogen adsorption, fluorescence is compatible with *in-situ* studies of wet gels and this gives it a major advantage. As an example we have used the new donor–acceptor distribution analysis presented in Sect. 3.4 in FRET studies of the drying of a 12.6% SiO_2 sol at pH 0.8 with a t_g of 240–270 mins. For this work we chose 10^{-5} M rhodamine

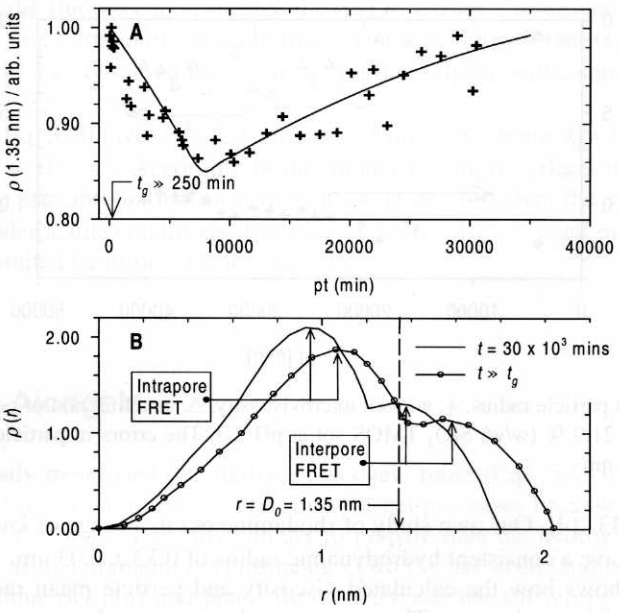

Fig. 3.6. A Measured donor-acceptor distribution function $\rho(r)$ at 1.35 nm for rhodamine 800-Cu^{2+} for an acidic gel drying at room temperature. The t_g was 240–270 mins. **B** Theoretical $\rho(r)$ for a two pore model, assuming the donor is located on the wall of one pore and the acceptors are randomly distributed throughout the same pore and an adjacent pore. Both intra- and inter-pore FRET are depicted in both curves as the gel dries and shrinks. The separation $r = 1.35$ nm corresponding to Fig. 3.6A is also shown

800 as the donor and 0.01M Cu^{2+} as the acceptor. This donor-acceptor pair has a D_0 value of 1.35 nm which is compatible with the pore size expected from the 4 nm particles in this sol (see Fig. 3.3), is minimally intrusive and FRET has been previously demonstrated in metal ion sensors [34, 35].

Fig. 3.6 shows how the donor-acceptor distance distribution function ρ(1.35 nm), determined using the procedures outlined in Sect. 3.4, changes during polymerisation, most of the time being occupied by the gel drying well after t_g. Essentially, the measurement sweeps out distribution information on a sphere of radius 1.35 nm and this is shown in Fig. 3.6A. A simulation of the theoretical $\rho(r)$ for a two pore model assuming the donor is located on the wall of one pore and the acceptors are randomly distributed throughout the same pore and an adjacent pore is shown in Fig. 3.6B as the gel shrinks. The dip in ρ(1.35 nm) shown in Fig. 3.6A can be interpreted as a reduction in the intra-pore acceptor site density detected as the measurement window at 1.35 nm moves outside the donor pore and into the wall between the pores and the increase at $t > 10{,}000$ mins reflects more acceptors in the adjacent pore moving into the measurement window. Fig. 3.7 depicts the two pore model we have used and the sizes obtained on analysing Fig. 3.6 A, assuming an exponential decrease as the gel dries and shrinks. The mean

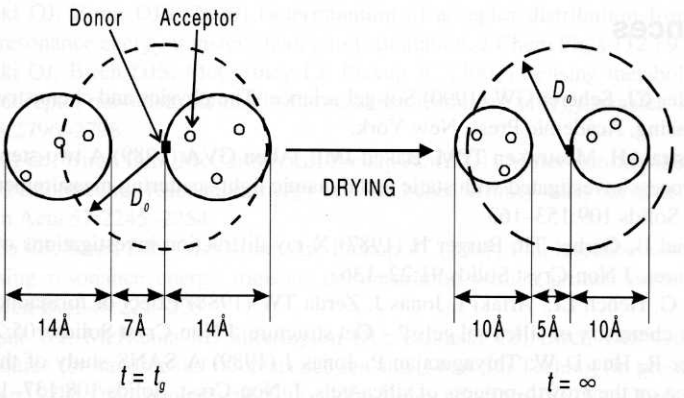

Fig. 3.7. Pore and wall dimensions found from the analysis of Fig. 3.6A as the gel dries

pore diameter is seen to reduce from 14 Å to 10 Å and the intervening silica wall thickness from 7 Å to 5 Å. The shrinkage rate constant is found to be ~ 4.8×10^{-7} s^{-1} and the volume change agrees well with that found from nitrogen adsorption measurements.

3.9 Conclusions

In this chapter we have illustrated the scope fluorescence offers for studying sol-gel processes under a wide range of experimental conditions and for different types of sols. Yet we have only scratched the surface of the rich science to be found in sol-gel transitions and much remains to be done. For example, everything we have reported here concerns a distribution of sizes of particles and pores and for each size a different rate equation pertains. We have so far been only able to address the mean and of course the distribution will influence the overall rates. Moreover, many processes can be simultaneous depending on conditions for example, hydrolysis and condensation, monomer addition and dissolution, particle aggregation and syneresis, etc.

Fluorescence nanoparticle metrology in sol-gels is only just beginning, but the signs are already promising that the full "kinetic life-history" of silica gel can be resolved over its range of reaction pathways. This should in turn lead to closer chemical control and if not new gel compositions then certainly better defined ones will be possible.

Acknowledgement. The authors wish to acknowledge the support of EPSRC and Ineos Silica Ltd.

References

1. Brinkler CJ, Scherer GW (1990) Sol-gel science: The physics and chemistry of sol-gel processing, Academic Press, New York.
2. Boonstra AH, Meeuwsen TPM, Baken JME, Aben GVA (1989) A two-step silica sol-gel process investigated with static and dynamic light-scattering measurements. J Non-Cryst Solids 109:153–163
3. Himmel B, Gerber Th, Burger H (1987) X-ray diffraction investigations of silica-gel structures. J Non-Cryst Solids 91:22–136
4. Orcel G, Hench LL, Artaki I, Jonas J, Zerda TW (1988) Effect of formamide additive on the chemistry of silica sol gels 2 – Gel structure. J Non-Cryst Solids 105:223–231
5. Winter R, Hua D W, Thiyagarajan P, Jonas J (1989) A SANS study of the effect of catalyst on the growth-process of silica-gels. J. Non-Cryst. Solids 108:137–142
6. Thompson NL (1991) Fluorescence correlation spectroscopy. In: Lakowicz JR (ed) Topics in fluorescence spectroscopy, vol 1: Techniques, Plenum, New York, pp 337–410
7. Birmingham JJ, Hughes NP, Treloar R (1995) Diffusion and binding measurements within oral biofilms using fluorescence photobleaching recovery methods. Phil Trans Royal Soc Lon B: Bio Sci 350:325–343
8. Birch DJS, Geddes CD (2000) Sol-gel particle growth studied using fluorescence anisotropy: An alternative to scattering techniques. Phys Rev E 62:2977–2980
9. Geddes CD, Birch DJS (2000) Nanometre resolution of silica hydrogel formation using time-resolved fluorescence anisotropy. J Non-Cryst Solids 270:191–204
10. Steiner RF (1991) Fluorescence anisotropy: theory and applications. In: Lakowicz JR (ed) Topics in fluorescence spectroscopy, vol 2: Principles, Plenum, New York, pp 1–51
11. Dunn B, Zink JI (1997) Probes of pore environment and molecule – matrix interactions in sol-gel materials. Chem Mater 9:2280–2291
12. Winter R, Hua DW, Song X, Mantulin W, Jonas J (1990) Structural and dynamical properties of the sol-gel transition. J Phys Chem 94:2706–2713
13. Dunn B and Zink JI (1991) Optical properties of sol-gel glasses doped with organic molecules. J Mater Chem 1:903–913
14. Narang U, Wang R, Prasad PN, Bright FV (1994) Effect of aging on the dynamics of rhodamine 6G in tetramethylorthosilicate-derived sols. J Phys Chem 98:17–22
15. Qian G, Wang, M (1999) Study on the microstructural evolution of silica gel during sol-gel-gel-glass conversions using fluorescence polarization of rhodamine B. J Phys D: Appl Phys 32:2462–2466
16. Blumen A, Klafter J, Zumofen G (1985) Influence of restricted geometries on the direct energy transfer. J Chem Phys 84:1397–1401
17. Pines-Rojanski D, Huppert D, Avnir D (1987) Pore-size effects on the fractal distribution of adsorbed acceptor molecules as revealed by electronic energy transfer on silica surfaces. Chem Phys Lett 139:109–115
18. Levitz P, Drake J M (1987) Direct energy transfer in restricted geometries as a probe of the pore morphology of silica. Phys Rev Lett 58:686–689
19. Levitz P, Drake JM, Klafter J (1988) Critical evaluation of the application of direct energy transfer in probing the morphology of porous solids. J Chem Phys 89:5224–5236

20. Rolinski OJ, Birch DJS (2000) Determination of acceptor distribution from fluorescence resonance energy transfer: theory and simulation. J Chem Phys 112:8923–8933
21. Rolinski OJ, Birch DJS, McCartney LJ, Pickup JC (2001) Sensing metabolites using donor-acceptor nanodistributions in fluorescence resonance energy transfer. Appl Phys Lett 78:2796–2798
22. Rolinski OJ, Birch DJS, McCartney LJ, Pickup JC (2001) Molecular distribution sensing in a fluorescence resonance energy transfer based affinity assay for glucose. Spectrochim Acta 57:2245–2254
23. Rolinski OJ, Birch DJS, McCartney LJ, Pickup JC (2001) Fluorescence nanotomography using resonance energy transfer: demonstration with a protein-sugar complex. Phys Med Biol 46:221–226
24. O'Hagan WJ, McKenna M, Sherrington DC, Rolinski OJ, Birch DJS (2001) MHz LED source for nanosecond fluorescence sensing. Meas Sci Technol (in press)
25. Iler RK (1979) The Chemistry of Silica, John Wiley and Sons Inc, New York
26. Birch DJS (2001) Multiphoton excited fluorescence spectroscopy of biomolecular systems. Spectrochim Acta A 57:2313–2336
27. Drexhage KH, Marx NJ, Arden-Jacob J (1997) New fluorescent probes for the red spectral region. J Fluorescence 7:91S–93S
28. Birch DJS, Imhof RE (1991) Time domain fluorescence spectroscopy using time-correlated single-photon counting. In: Lakowicz JR (ed) Topics in fluorescence spectroscopy, vol 1: Techniques, Plenum, New York, pp 1–95
29. Karolin J, Geddes CD, Wynne K, Birch DJS (2001) Nanoparticle metrology in sol-gels using multiphoton excited fluorescence. Meas Sci Technol (in press)
30. Volkmer A, Hatrick DA, Birch DJS (1997) Time-resolved nonlinear fluorescence spectroscopy using femtosecond multiphoton excitation and single-photon timing detection. Meas Sci Technol 8 (11):1339–1349
31. Fischer A, Cremer C, Stelzer EHK (1995) Fluorescence of coumarins and xanthenes after two-photon absorption with a pulsed titanium-sapphire laser. Appl Opt 34:1989–2003
32. Albota MA, Xu C, Webb WW (1998) Two-photon fluorescence excitation cross sections of biomolecular probes from 690 to 960 nm. Appl. Opt. 37:7352–7356
33. Porter G, Sadkowski PJ, Tredwell CJ (1977) Picosecond rotational diffusion in kinetic and steady state fluorescence spectroscopy. Chem Phys Lett 49:416–420
34. Birch DJS, Rolinski OJ, Hatrick D (1996) Fluorescence lifetime sensor of copper ions in water. Rev Sci Instrum 67:2732–2737
35. Birch DJS, Rolinski OJ (2001) Fluorescence resonance energy transfer sensors. Res Chem Int 27:425–446